A revised model for rubbing between rotating blade and elastic casing

Hui Ma, Xingyu Tai, Qingkai Han, Zhiyuan Wu, Di Wang, Bangchun Wen

A revised model for rubbing between rotating blade and elastic casing

Hui Ma [a], Xingyu Tai [b], Qingkai Han [c], Zhiyuan Wu [a], Di Wang [a], Bangchun Wen [a]

[a] School of Mechanical Engineering and Automation, Northeastern University, Shenyang, Liaoning 110819, PR China
[b] Shenyang Blower Works Group Corporation, Shenyang, Liaoning 110869, PR China
[c] School of Mechanical Engineering, Dalian University of Technology, Dalian, Liaoning 116023, PR China

In this paper, a new rubbing model between a rotating blade and elastic casing is derived based on the law of conservation of energy. In this model, the bending deflection of blade and the casing deformation during rubbing are taken into account. Based on this model, the influences of the penetration depth, casing stiffness, friction coefficient, blade physical dimensions (thickness, width and length) on the quasi-static normal rubbing forces are analyzed. Moreover, the effects of blade types (thin, thick and tapered blades), casing stiffnesses (aluminum and steel casings), penetration depths and rotating speeds on the normal rubbing forces are also evaluated by simulation and experiment. Moreover, by establishing the dynamic model of the blade and casing, the dynamic normal rubbing forces are also calculated under the blade-casing rubbing. The results show that the rubbing model has satisfactory accuracy by comparing simulation with experiment; the linear or nonlinear characteristic of normal rubbing force depends on the stiffnesses of the blade and the casing; the dynamic normal rubbing force is less than the quasi-static normal rubbing force, and both have the same change trend.

1. Introduction

In aeroengine or gas turbine, in order to improve the energy efficiency it is common practice to reduce the tip clearance between the rotating blade and the stationary casing. However, as the clearance reduces, the probability of the rubbing occurring under some operational conditions also increases. Blade-casing rubbing has long been identified as a significant contributor to excessive maintenance and in general to engine failure. The rubbing may result in complicated vibration of the overall unit, and may lead to reduced system performance and reduce the lives of the blade and the casing.

Due to the complexity of the rubbing phenomenon, many researchers carried out some outlooks on rotor -stator/blade-casing interactions. A list of review articles have addressed this issue, such as Muszynska [1], Ahmad [2], Chen and Zhang [3], Jiang and Chen [4], Jacquet-Richardet et al. [5]. Muszynska [1] presents a literature survey on rub-related phenomena in rotating machinery, such as friction, impacting, stiffening and coupling effects. Ahmad [2] provides an overview of the state of the art on the rotor-casing contact phenomenon in rotor dynamics and describes aspects of different physical parameters

Nomenclature

A_0	cross-section area at the root of the blade
A	cross-section area of the blade
b_0, b_1	width at the root and the tip of the blade
c_c	damping of casing
$\mathbf{D}_b$	damping matrix of blade
E	Young's modulus
$\mathbf{F}$	canonical external force vector of blade
F_e	aerodynamic force in y direction
F_n	normal rubbing force at the tip of the blade
F_t	tangential rubbing force at the tip of the blade
f_c	centrifugal force
$\mathbf{G}_b$	Coriolis force matrix of blade
G	shear modulus
h_0, h_1	height at the root and the tip of the blade
I_0	cross-section inertia moment at the root of the blade
I	cross-section inertia moment of the blade
$\mathbf{K}_e$	structural stiffness matrix of blade
$\mathbf{K}_c$	stress stiffening matrix of blade
$\mathbf{K}_s$	spin softening matrix of blade
$\mathbf{K}_{\text{acc}}$	stiffness matrix of blade caused by acceleration
$\mathbf{K}_F$	stiffness matrix of blade caused by external force
k_c	equivalent stiffness of the casing
L	blade length
$\mathbf{M}_b$	mass matrix of blade
m_c	mass of casing
$\mathbf{q}_b$	canonical coordinates vector of blade
R_c	radius of the casing
R_d	radius of the disk
T	kinetic energy of the blade
T_r	bending moment at blade tip
U_c	centrifugal potential energy
U_e	bending potential energy
$U_i(t)$, $V_i(t)$ and $\psi_i(t)$	canonical coordinates
u, v, φ	radial displacement, lateral displacement, shear angle
u_c	displacement of the casing in X direction
u_L	radial displacement caused by bending at the blade tip
V	potential energy of the blade
v_L	bending displacement at the blade tip
W	work done by normal force F_n and tangential force F_t at the tip of the blade
W_{non}	work done by non-conservative force applied the blade
w	displacements in swing directions of the blade

Greek symbols

δ	penetration depth
δ_1	dynamic penetration depth
$\delta_{\max}$	maximum penetration depth
θ	rotation angular of the disk motion
κ	shear correction factor
μ	friction coefficient
ρ	material density
τ_b, τ_h	taper ratios along the width and height directions
$\phi_{1i}(x)$, $\phi_{2i}(x)$, $\phi_{3i}(x)$	modal shape function
φ_1	phase position
Ω	rotating angular velocity

such as stiffness, damping, Coulomb friction, acceleration of rotor, support structure asymmetry, thermal effects and disk flexibility etc. Chen et al. [3] present an overview of the researches on the dynamics of complete aero-engine systems in recent years including the dynamics analysis of the rubbing of the rotor-casing system. Jiang et al. [4] summarize the literature on the rotor/stator rubbing in the past half century from view of dynamics and control and classify the existing modeling on the rotor/stator rubbing into two categories: the local rubbing models and the system rubbing models. Moreover, the authors also discuss the progress in the study of synchronous rubbing responses, sub-harmonic and super-harmonic rubbing responses, quasi-periodic partial rubbing, dry whirl/whip, coexistence of multi-stable rubbing responses as well as bifurcation and chaos of rubbing responses and also summarize the ideas and results of passive and active suppression of rubbing in the literature. Jacquet-Richardet et al. [5] evaluate the main works published on the problem of contact between fixed and moving parts of turbomachines, by focusing on the two principal configurations involving contact, namely blade-casing and rotor-stator. Their analysis also examines existing numerical models and experimental setups and highlights the phenomenology involved during contacts.

In Ref. [1], Muszynska also indicates that most often rub occur at seals; seldom, but more blade rubs against the stator or vane may be experienced. In most research, the rotor-stator rubbing has been simulated by the contact between two concentric cylindrical surfaces represented the rotor and the stator, respectively [6]. The linear spring model is usually adopted to describe the normal rubbing force F_n and the radial penetration depth δ, which can be expressed by the linear collision force relation.

$$F_n = k_s \delta, \tag{1}$$

where k_s is the stator stiffness.

Jiang et al. [4] show that it is known that rubbing often occurs at seals and the blade-casing rubbing occurs much less frequently, but the latter is more dangerous than the former due to higher line velocity at blade tip and larger impact energy, which also has a great influence on the rotor dynamics. Blade-casing rubbing is a more complicated impact process: (a) collision occurs between the flexible body and elastic body with a relatively large stiffness or two flexible bodies (the casing is thin shell), here the impact force mainly depends on the whole deformation of flexible body rather than the local

deformation; (b) the blade-casing rubbing is a oblique collision when there is a certain angle between the blade tip and the line velocity, which easily causes the bending-torsion coupling deformation of the blade; (c) the impact is not transient during the rubbing process due to the obvious movement of the blade tip location. For blade rubbing, by assuming the blade as the cantilever beam, Padovan and Choy [7] deduce the relationship between the normal contact force and the radial deformation of blade and analyze the nonlinear dynamic characteristics of system under single blade and multi blades rubbing conditions. The normal blade-casing rubbing force F_n under the single blade rubbing condition is presented as follows:

$$F_n = \frac{\pi^2}{4}\frac{EI}{L^2}\frac{(\pi/2)\sqrt{\delta/L}}{\mu+(\pi/2)\sqrt{\delta/L}}, \tag{2}$$

where E, I, L, δ, and μ are Young's modulus, cross-section inertia moment of the blade, length of the blade, penetration depth and the friction coefficient, respectively. Considering the stiffening effect due to the rotation of the blade, Jiang et al. [8] deduce the normal rubbing force between the rotating blade and casing based on Padovan's model. The revised expression is as follows:

$$F_n = 2.5\frac{EI}{L^2}\frac{1.549\sqrt{\delta/L}}{\mu+1.549\sqrt{\delta/L}}+\frac{11}{56}\rho AL\Omega^2\left(\frac{5}{22}L+\frac{35}{22}R\right)\frac{1.549\sqrt{\delta/L}}{\mu+1.549\sqrt{\delta/L}}, \tag{3}$$

where ρ is the material density, A the cross section area of blade, Ω the rotating angular velocity, R the radius of the disk and the other parameters are same as those in Eq. (2).

Aiming at the blade-casing rubbing problem, model experimentation is also widely used, which can verify the theoretical results, find some new experimental phenomena and make up for the lack of the theoretical models. By simplifying the blade as a rotating uniform beam and the casing as an arc structure, which can be adjusted between 0 and 90° to the direction of the motion of the blade, Ahrens et al. [6] carries out experiments on contact forces and the duration of contact. They measure the time histories of the normal and tangential forces during the contact of the blade with the casing and also examine the influence of the friction and the rubbing speed on the contact force. Padova et al. [9–11] develop an in-ground spin-pit facility which is capable of rotating at engine speed and can simulate compressor blade rubbing bare-steel and treated casings at engine speed. In spin-pit facility, the shaft is driven on the top by a reversible air motor. A 90° sector of a representative engine casing is forced to rub the tip of a single-bladed compressor disk at a selected number of rubs with predetermined blade incursion into the casing. Contact force is measured by tree triaxial piezoelectric force transducers and vibrations caused by contact are obtained by five accelerometers. The blade is equipped with deformation gauges and a thermocouple, and an electric circuit is used to determine the collision times. In Ref. [11], Padova et al. indicate that in the linear region (see Fig. 1), the elastic deformations of the blade dominate the rub dynamic. As the interference δ (penetration depth) increases along the rub arc, the blade displaces away from the interfering shroud surface by bending and some slipping and elastic deformation at the dovetail. In the transition region, the behavior of the “equivalent” spring becomes nonlinear as the allowed blade movements are again and again maxed out and other mechanisms material abrasion and plastic deformation are among them come into play to compensate for a more severe interference. In the asymptotic region, plastic deformations and grinding at the blade tip dominate the rub dynamics.

The above blade-casing rubbing model assumes that the casing is rigid. For the ground-based gas turbines, the assumption is reasonable. However, for an aircraft engine, the casing thickness is about 1–2 mm and its stiffness is also much smaller. Therefore, the casing deformation is also larger in the process of rubbing between the blade and the casing. So aiming at the aircraft engine, the rubbing models considering the rigid casing should be revised to make up for disadvantages of the existing models. In this study, the main object is to present a revised blade-rubbing rubbing model based on Jiang's model considering the effect of the elastic casing. Moreover, the revised model is also verified by experiment.

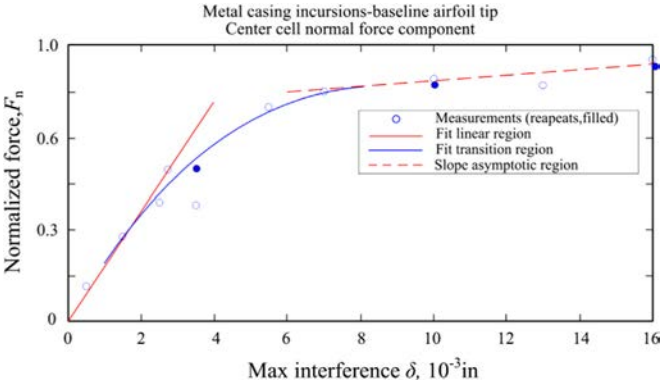

Fig. 1. Recorded loads, group 1 (steel casing) [11].

This paper consists of four sections. A mathematic rubbing model is derived in Section 2.1 and parameter effects on the normal rubbing force are discussed in Section 2.2. In Section 3.1, experiment facilities are introduced, and the comparation of simulation and experiment is described in Section 3.2. Dynamic normal rubbing force is analyzed under the blade-casing rubbing in Section 4. Finally, discussion and outlook are provided in Section 5.

2. Mathematic model for blade-casing rubbing

2.1. Mathematic model derivation based on work-energy theorem

Generally, different normal rubbing models have less influence on the dynamic behaviors of the rotor and stator under reasonable stator stiffness conditions, however, the quantitative rubbing force has a great effect on the abrasion effects and local deformations of the rotor and stator [4]. So it is very important to accurately estimate the rubbing force.

The rubbing may occur between the flexible body and elastic body with a relatively large stiffness or two flexible bodies (the casing is thin shell), here the impact force mainly depends on the whole deformation of flexible body rather than the local deformation [4]. So the normal rubbing force between the blade and elastic casing is closely related to the blade and casing deformations during the collision process (see Fig. 2). In order to study conveniently, some simplifications about the normal rubbing process are introduced as follows:

(a) Ignoring the kinetic energies of the blade and casing, the blade-casing rubbing process is simplified as a quasi-static contact process;
(b) The axial compression potential energy cause by rubbing is neglected, and only bending potential energy and potential energy caused by centrifugal force are considered;
(c) The deflection of the disk is neglected, namely, the disk is rigid, and the blade is considered to be a cantilever beam, the material of the blade is homogeneous and isotropic;
(d) Thermal effects during rubbing are not considered.

Assuming that the blade-section is variable along the longitudinal direction, the cross-section area and cross-section inertia moment of the blade can be expressed as

$$\begin{cases} A(x) = A_0\left(1-\tau_b\frac{x}{L}\right)\left(1-\tau_h\frac{x}{L}\right) \\ I(x) = I_0\left(1-\tau_b\frac{x}{L}\right)\left(1-\tau_h\frac{x}{L}\right)^3 \end{cases}, \tag{4}$$

where $A_0 = b_0 h_0$ and $I_0 = (1/12) b_0 h_0^3$ are the cross sectional area and cross-section inertia moment at the root of the blade, respectively; $\tau_b = 1-(b_1/b_0)$ and $\tau_h = 1-(h_1/h_0)$ are the taper ratios along the width and height directions. Here, b_1 and h_1 are the width and height at the tip of the blade; b_0 and h_0 are the width and height at the root of the blade.

The energy balance during contact between the blade and casing can be expressed as

$$U_e + U_c = W, \tag{5}$$

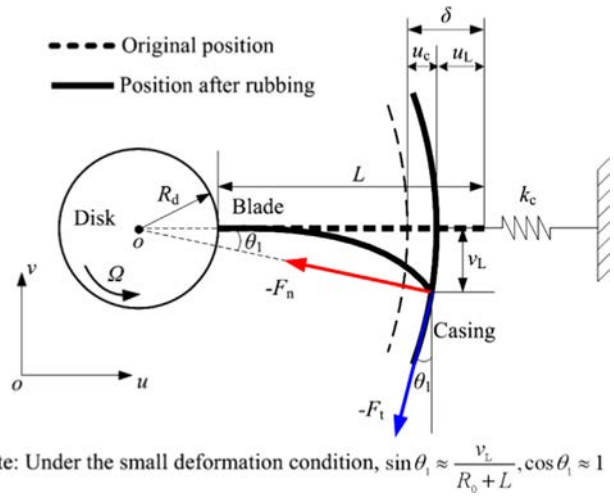

Fig. 2. Schematic of rubbing between single blade and elastic casing.

where U_e is the bending potential energy, defined by

$$U_e = \frac{1}{2}\int_0^L EI(x)\left(\frac{\partial^2 v}{\partial x^2}\right)^2 dx, \tag{6}$$

here, E, L and v are Young's modulus, blade length and the lateral displacement of blade, respectively. U_c is the centrifugal potential energy, defined by

$$U_c = \frac{1}{2}\int_0^L \frac{1}{2}\rho A(x)\Omega^2\left(L^2 + 2R_d L - 2R_d x - x^2\right)\left(\frac{\partial v}{\partial x}\right)^2 \mathrm{d}x, \tag{7}$$

where ρ, R_d and Ω are the density of the blade, radius of the disk and the rotating angular velocity, respectively. W is the work done by normal force F_n and tangential force F_t at the tip of the blade, herein the tangential force F_t is the force of friction between the blade and casing, which is simulated by Coulomb friction model, i.e. $F_t = \mu F_n$, where μ is the friction coefficient:

$$W = \frac{1}{2}F_t \cos\theta_1 v_L - \frac{1}{2}F_n \sin\theta_1 v_L = \frac{1}{2}\mu F_n v_L - \frac{1}{2}\frac{v_L^2}{R_d + L}F_n. \tag{8}$$

Here, v_L is the bending displacement at the blade tip.

Assuming that the casing during contact has a linear stiffness, the contact force can be written as

$$F_{\text{elastic}} = k_c u_c, \tag{9}$$

where k_c and u_c are the equivalent stiffness and the radial displacement of the casing. The force balance relation is shown in Fig. 3, which can be obtained by

$$F_n = F_{\text{elastic}}.$$

Assuming that there is a quasi-static deformation equilibrium state at any time during rubbing, the geometrical relation between the penetration depth and the radial displacement of the casing (see Fig. 2) can be expressed as follows:

$$\delta = u_L + u_c. \tag{10}$$

Here, u_L is the radial displacement at the blade tip, given by

$$u_L = \frac{1}{2}\int_0^L \left(\frac{\partial v}{\partial x}\right)^2 \mathrm{d}x. \tag{11}$$

Based upon the fundamental theory of material mechanics, the deformation of cantilever blade with constant or variable section can be approximately expressed as [12]

$$v = v_L\frac{1}{2}\left(\frac{3x^2}{L^2} - \frac{x^3}{L^3}\right). \tag{12}$$

Substituting Eq. (12) into Eqs. (6) and (7), based on Eq. (5), the expression of the bending displacement at the blade tip v_L is written as

$$v_L = \frac{\mu F_n}{\Gamma_0 + (F_n/(R_d + L))}, \tag{13}$$

where

$$\Gamma_0 = EI_0\left(\frac{3}{L^3} + A_1\right) + \rho A_0\Omega^2\left(\frac{81}{280}L + \frac{3}{8}R_d + A_2\right).$$

Here, the expressions of A_1 and A_2 are defined as

$$A_1 = -\frac{3\tau_b}{4L^3} - \frac{9\tau_h}{4L^3} + \frac{9\tau_b\tau_h}{10L^3} + \frac{9\tau_h^2}{10L^3} - \frac{9}{20L^3}\tau_b\tau_h^2 - \frac{3}{20L^3}\tau_h^3 + \frac{3}{35L^3}\tau_b\tau_h^3,$$
$$A_2 = -\frac{369}{2240}L\tau_b - \frac{57}{280}R_d\tau_b - \frac{369}{2240}L\tau_h - \frac{57}{280}R_d\tau_h + \frac{59}{560}L\tau_b\tau_h + \frac{141}{1120}R_d\tau_b\tau_h.$$

Then u_L can be obtained by Eqs. (11) and (12). Substituting the expressions of u_L and $u_c = F_n/k_c$ into Eq. (10), the penetration depth δ can be expressed as

$$\delta = \frac{3\mu^2(L + R_d)^2F_n^2}{5L(F_n + (L + R_d)\Gamma_0)^2} + \frac{F_n}{k_c}. \tag{14}$$

Neglecting the high-order terms, the expression of F_n can be obtained.

$$F_n = \frac{-5\Gamma_0 L\left(((R_d + L)/L)(\Gamma_0/k_c) - 2(\delta/L)\right) + \sqrt{5}(R_d + L)\Gamma_0\sqrt{5(\Gamma_0/k_c)\left((\Gamma_0/k_c) + 4(L/(R_d + L))(\delta/L)\right) + 12\mu^2(\delta/L)}}{20(\Gamma_0/k_c) - 10(L/(R_d + L))(\delta/L) + 6((R_d + L)/L)\mu^2}. \tag{15}$$

Finally, the expression of F_n can be written as

$$F_n = L\Gamma_1 k_c \frac{-5(\alpha\Gamma_1 - 2(\delta/L)) + \sqrt{5}\alpha\sqrt{5\Gamma_1(\Gamma_1 + (4/\alpha)(\delta/L)) + 12\mu^2(\delta/L)}}{20\Gamma_1 - (10/\alpha)(\delta/L) + 6\alpha\mu^2}, \tag{16}$$

where $\Gamma_1 = \Gamma_0/k_c$, $\alpha = (R_d + L)/L$.

When the stiffness of the casing is large, and the deformation of the casing is neglected, i.e. $u_c = 0$ in Eq. (10). Then the quasi-static normal rubbing force can be expressed as

$$F_n = \Gamma_0 L \frac{5((R_d + L)/L)(\delta/L) + \sqrt{15}((R_d + L)/L)^2\mu\sqrt{\delta/L}}{-5(\delta/L) + 3((R_d + L)/L)^2\mu^2}. \tag{17}$$

When the stiffness of the casing is small and then the radial deformation of the blade is neglected. The quasi-static normal rubbing force in this condition can be written as

$$F_n = k_c\delta. \tag{18}$$

The expressions of the normal rubbing force in Eqs. (17) and (18) can be regarded as two limiting cases. If the deformation of the blade is much larger, the F_n shows the nonlinear characteristic against the penetration depth, which is related to rotating speed, friction coefficient, physical dimensions and material parameters of blade and disk (see Eq. (17)).

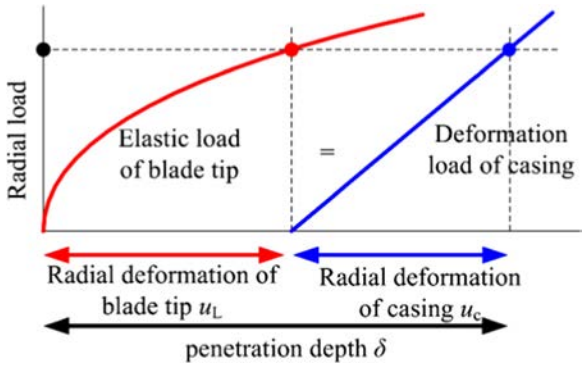

Fig. 3. Force balance schematic during rubbing.

Table 1
Parameters of the blade and disk.

Parameter	Value	Parameter of blade	Value	Parameter of disk	Value
Young's modulus E (GPa)	200	Blade length L (mm)	82	Radius of the disk R_d (mm)	140
Density ρ (kg/m^3)	7800	Blade width b (mm)	44		
Poisson's ratio υ	0.3	Blade thickness h (mm)	3		

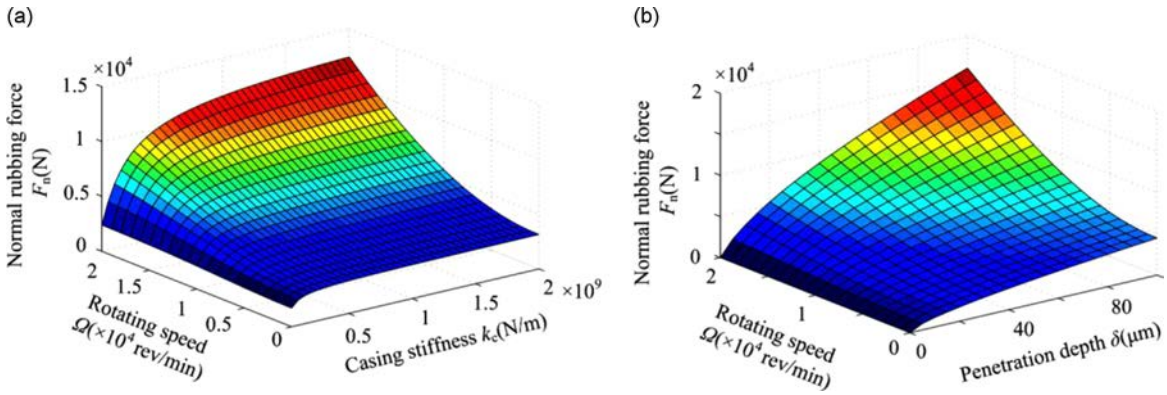

Fig. 4. Quasi-state normal rubbing force under different parameters: (a) parameters of rotating speed and casing stiffness, (b) parameters of rotating speed and penetration depth.

If the deformation of the casing is much larger, the F_n shows linear relationship with the penetration depth and the slope is the casing stiffness (see Eq. (18)).

2.2. Parameter effects on the quasi-static normal rubbing force

The parameters of the blade and disk are shown in Table 1. The effects of the rotating speed Ω, penetration depth δ, casing stiffness k_c, friction coefficient μ and physical dimensions of blade (length L, width b and thickness h) on the quasi-static normal rubbing force are discussed in this section.

The quasi-static normal rubbing forces changing with the casing stiffness and penetration depth are shown in Fig. 4 under different rotating speeds. This figure indicates the following characteristics of the normal rubbing force:

(1) When the casing stiffness is smaller, the normal rubbing force almost remains unchanged with the increasing rotating speed. The normal rubbing force presents the "hard" characteristic as the rotating speed increases under larger casing stiffness. However, the normal rubbing force displays the "soft" characteristic with the increasing casing stiffness (see Fig. 4a). These change laws are similar to those shown in Fig. 1.
(2) The normal rubbing force increases with the increasing penetration depth and presents the "soft" characteristic. Moreover, the normal rubbing force changing with rotating speed also presents the "hard" characteristic under larger penetration depth (see Fig. 4b).

The normal rubbing forces changing with the casing stiffness and friction coefficient under different penetration depths are shown in Fig. 5, which indicates the characteristics of the normal rubbing force as follows:

(1) The normal rubbing force keeps in a certain value after the casing stiffness increases to larger value and the effect of the casing stiffness is more obvious under larger penetration depth. When the casing stiffness is small, the linear relation between the normal rubbing force and the penetration depth is expressed and a nonlinear "soft" characteristic can been seen in large casing stiffness (see Fig. 5a). These changes can be explained by Eqs. (17) and (18).

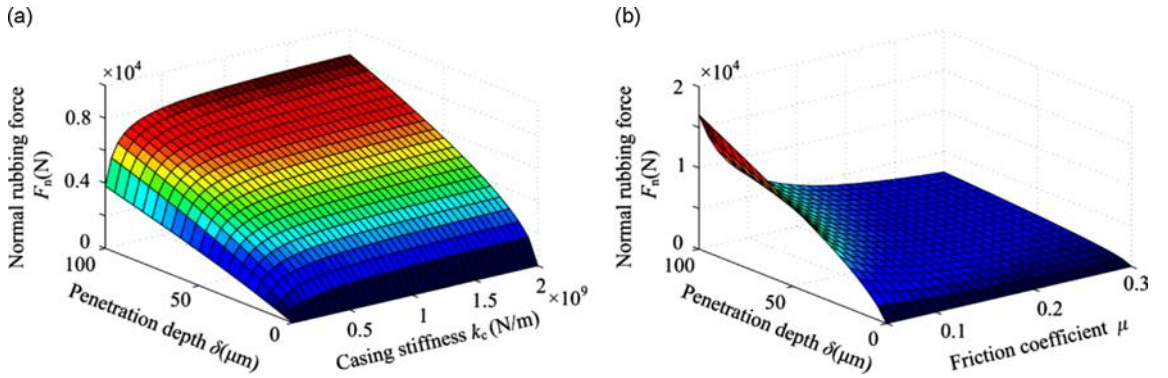

Fig. 5. Normal rubbing force under different parameters: (a) parameters of penetration depth and casing stiffness, (b) parameters of penetration depth and friction coefficient.

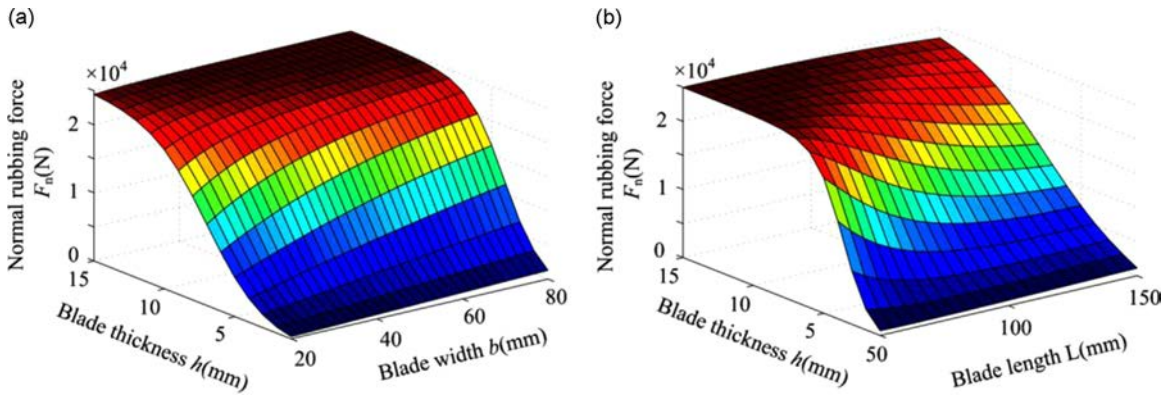

Fig. 6. Normal rubbing force under different parameters: (a) parameters of blade thickness and blade width, (b) parameters of blade thickness and blade length.

(2) The normal rubbing force reduces with the increasing friction coefficient and reduces sharply when the friction coefficient is between 0 and 0.1 (see Fig. 5b). The normal rubbing force decreases slightly in the range of $\mu \in [0.1, 0.3]$. The reason causing this phenomenon is that μ is related to the tangential rubbing force (friction force) and it has influence on the deflection curve of the blade. The smaller friction coefficient μ is, the smaller deflections in tangential and normal directions are. Meanwhile, the displacement of the casing increases under constant penetration depth, thus the normal rubbing force is greater in order to balance the reactive force caused by the casing deformation. Under larger friction coefficient, such as in the range of $\mu \in [0.1, 0.3]$, the radial displacement of the blade increases slightly, therefore, the normal rubbing force decreases slightly.

The normal rubbing forces changing with the length, width and thickness of the blade are shown in Fig. 6. The figure displays the following characteristics of the normal rubbing force:

(1) The normal rubbing force increases slightly with the increasing blade width. Blade thickness has a great influence on the normal rubbing force. With the increasing blade thickness, the normal rubbing force increases obviously under small blade thickness range and gradually tends to stabilization under large blade thickness range. Comparing with the narrow blade, wide blade reaches the steady state in advance (see Fig. 6a).
(2) The normal rubbing force reduces with the increasing blade length. Comparing with the long blade, short blade reaches the steady state in advance (see Fig. 6b).

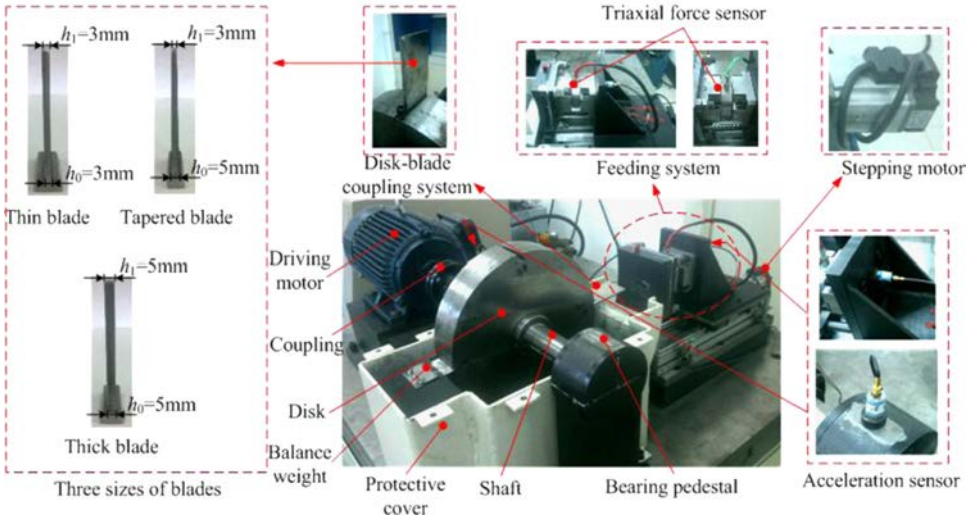

Fig. 7. Test rig for rubbing between the blade and casing.

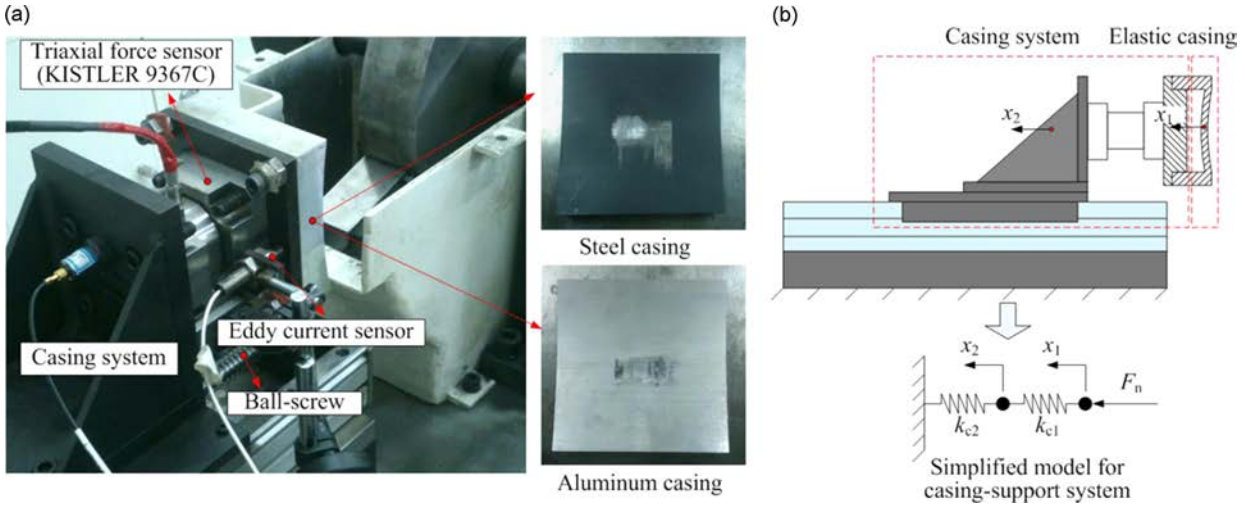

Fig. 8. Casing system: (a) casing structure, (b) simplified model of the casing system.

(3) Based on the qualitative analysis, it can be seen that the effects of blade thickness, blade length and blade width on normal rubbing force weaken successively. Normal rubbing force depends on the blade bending deflection extent caused by these parameters.

3. Model verification

3.1. Experiment facilities

A test rig (see Fig. 7) composed of the drive system, rotor system, feeding system and testing system, was established to verify the theoretical results. The drive system includes a motor and a coupling. The maximum rotating speed of the motor is 3000 rev/min. The rotor system consists of a rigid shaft and a rigid disk, which are used to reduce the effects of rotor vibration on blade-tip rubbing. The blade and the disk are connected by dovetail interface and a counter-weight on the opposite side of the blade is used to balance the rotor system. The rotor is mounted in two ball bearings and driven by the motor. To ensure safety, the rotor system is mounted in a protective cover. In this study, three sizes of steel blade (thin, tapered and thick blades) are used in experimental study.

The feeding system of this test rig includes a linear guide, which is driven by a stepping motor through a ball-screw with a feeding rate of 1 μm/step. An elastic casing is fixed on the linear guide, which is a sector of thin inner cylinder surface to simulate a part of the elastic casing (see Fig. 8) and its center is leveled with the rotor center. In this study, aluminum and steel casings are used to adjust different casing stiffness. The testing system includes a triaxial force sensor (KISTLER TYPE 9367C), two accelerometers and an eddy current sensor. The force sensor is used to measure the normal and tangential rubbing forces between the blade and the casing (see Fig. 8a). The accelerometer is adopted to measure the accelerations of the bearing and casing (see Figs. 7 and 8a). The eddy current sensor is used to measure the casing vibration displacement (see Fig. 8a). Before each test, the blade-casing gap is firstly adjusted to zero, which can assure the blade contact at the center of the casing at a given rotating speed. The rubbing intensity can be adjusted by increasing the penetration depth with a penetration rate of 1 μm/step. The experiment focuses on the effects of penetration depth, rotating speed and casing stiffness on the normal rubbing force.

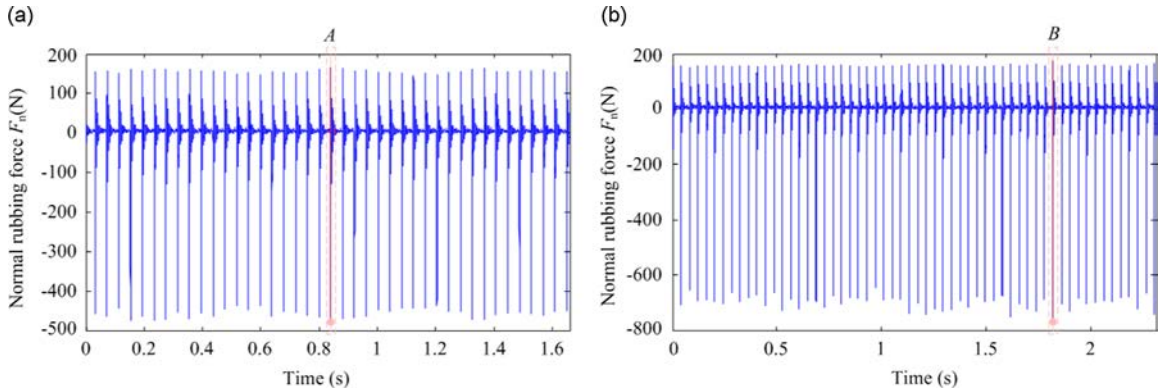

Fig. 9. Measured normal rubbing forces for thin blade (Ω=1500 rev/min, maximum penetration depth 50 μm): (a) aluminum casing, (b) steel casing.

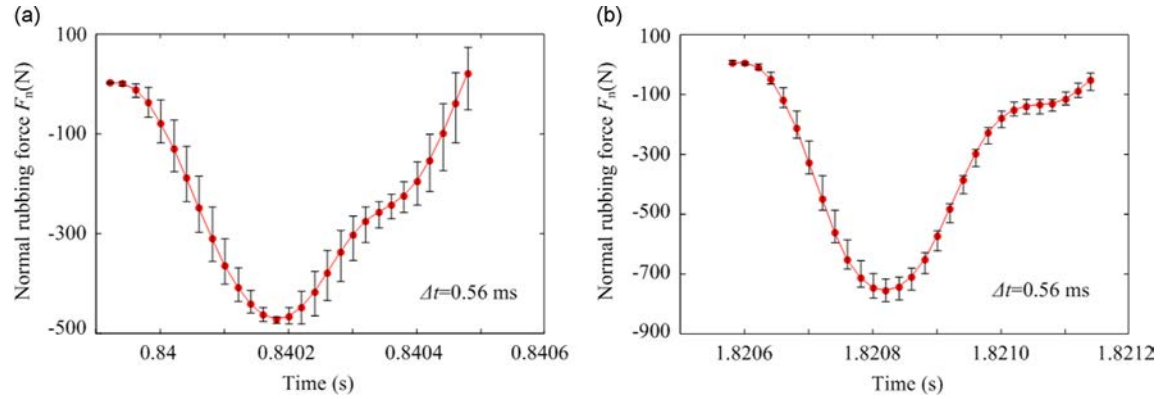

Fig. 10. Variation range of measured normal rubbing force for thin blade by multiple measurements (Ω=1500 rev/min, maximum penetration depth 50 μm): (a) moment *A* in Fig. 9, (b) moment *B* in Fig. 9.

3.2. Experimental results

3.2.1. Experimental results for the rubbing force

Measured normal rubbing forces for aluminum and steel casings are shown in Fig. 9 where the negative value denotes the normal rubbing force. The rubbing force which has the maximum amplitude is selected as research object, such as *A* and *B* in Fig. 9. Multiple repeated tests for this condition are carried out to ensure the stability and credibility of testing results. Measured results corresponding to moments *A* and *B* in Fig. 9 are shown in Fig. 10, which indicates that the test results are stable.

3.2.2. Experimental results for the friction coefficient

The friction coefficient μ can be obtained by the ratio of the amplitudes of the normal and tangential rubbing force [7]. For aluminum and steel casings, average friction coefficients for rotating speeds of 1000, 1500 and 2000 rev/min are measured. Friction coefficients of two casings are plotted with the changing normal rubbing force are shown in Fig. 11. The figure shows that the friction coefficient keeps stable near 0.063 for aluminum casing. For steel casing, the friction

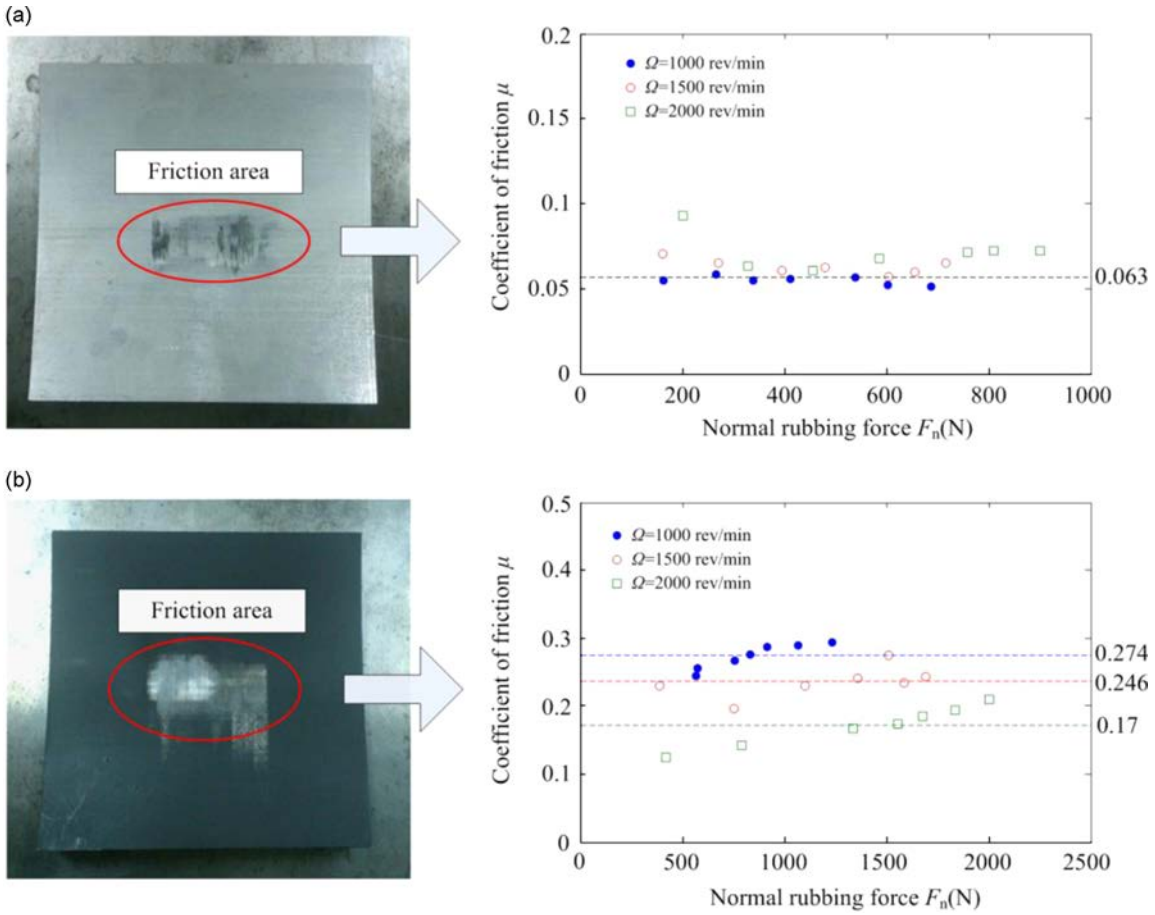

Fig. 11. Friction coefficient of two casings (thin blade): (a) aluminum casing, (b) steel casing.

Table 2
Average friction coefficients of the casings (thin blade).

Average friction coefficient					
Aluminium casing			Steel casing		
1000 rev/min	1500 rev/min	2000 rev/min	1000 rev/min	1500 rev/min	2000 rev/min
0.063	0.063	0.063	0.274	0.246	0.17

coefficient reduces with the increasing rotating speeds and changes from 0.274 at 1000 rev/min through 0.246 at 1500 rev/min to 0.17 at 2000 rev/min. Average friction coefficient of the casing are shown in Table 2 under different rotating speeds. Here, the friction coefficient of aluminum casing is very small because the friction surface becomes smooth in the process of repeated rubbing.

3.2.3. Experimental results for the casing stiffness

In view of the casing system including multiple parts, such as elastic casing, force sensor, etc., so the casing system stiffness (hereafter referred to as a casing stiffness) needs to consider the stiffness of each subsystem. A simplified model for casing-support system is shown in Fig. 8b. In the figure, x_1, k_{c1} and x_2, k_{c2} denote the displacements and stiffnesses of elastic casing and casing support system including force sensor, linear guide and guide screw, respectively. Assuming that the two subsystems are connected by series, the casing stiffness can be determined as follows:

$$k_c = \frac{k_{c1}k_{c2}}{k_{c1}+k_{c2}}. \tag{19}$$

Elastic casing and linear guide are fixed by guide screw with a certain rigidity. The displacement of the casing support system is assumed as x_2 under the action of normal rubbing force. Assuming that the casing is a linear system, the approximate stiffness of the casing can be determined by the ratio of measured normal rubbing force with the displacement x_2 (see Fig. 12). The stiffness of elastic casing can be approximately evaluated by the ratio of the force with the deformation based on finite element method. Stiffness ranges of different parts for the casing system are shown in Table 3. In this study, the steel casing stiffness k_c is assumed as 3.5×10^7 N/m and the aluminum casing stiffness is 2×10^7 N/m.

3.3. Comparison of simulation and experiment

3.3.1. Effects of different types of blades on the normal rubbing force

Simulated and measured normal rubbing forces between three types of blades and steel casing are shown in Fig. 13 under rotating speed of $\Omega = 1000$ rev/min. The figure shows the following dynamic phenomena:

(1) For the thin blade, the simulated result agrees well with the measured result, especially under the small penetration depth condition, such as $\delta \in [20, 60]$ μm. The experimental result is greater than the simulation result under large penetration depth.
(2) For the thick and tapered blades, the simulated and measured rubbing forces are very closely with each other. The simulated rubbing force of thick blade is largest because its bending stiffness is largest and measured results do not reflect this phenomenon due to the test error. The experimental results are always less than the simulation results and the difference of both reaches the maximum under largest penetration depth. The reason caused larger error is that the casing stiffness may change with the increasing penetration depths and the measured penetration depths may not be completely accurate.

Table 3
Stiffness ranges of different parts for the casing system.

Material	Aluminum	Steel
Stiffness of the elastic casing k_{c1} (N/m)	$4.17 \times 10^7 \sim 8.62 \times 10^7$	$1.42 \times 10^8 \sim 4.4 \times 10^8$
Stiffness of the casing-support system k_{c2} (N/m)	$3.64 \times 10^7 \sim 4.497 \times 10^7$	
Casing stiffness k_c (N/m)	$1.9435 \times 10^7 \sim 2.96 \times 10^7$	$2.8973 \times 10^7 \sim 4.08 \times 10^7$

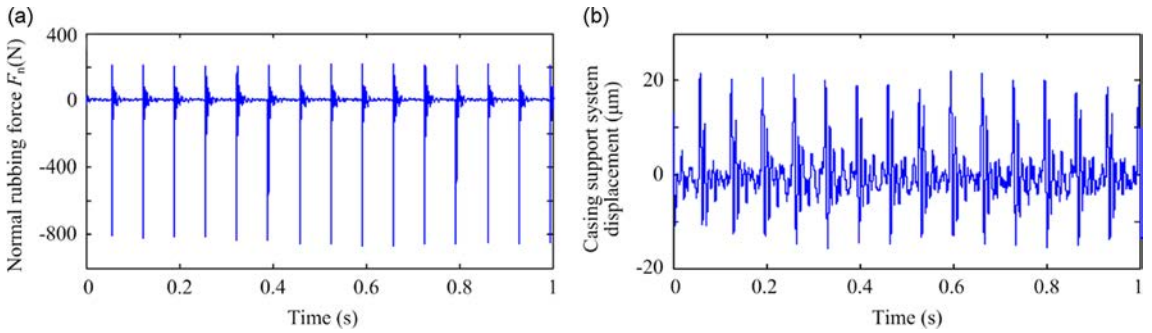

Fig. 12. Measured normal rubbing force and casing displacement for thin blade ($\Omega = 1000$ rev/min, steel casing): (a) normal rubbing force, (b) displacement of the casing support system.

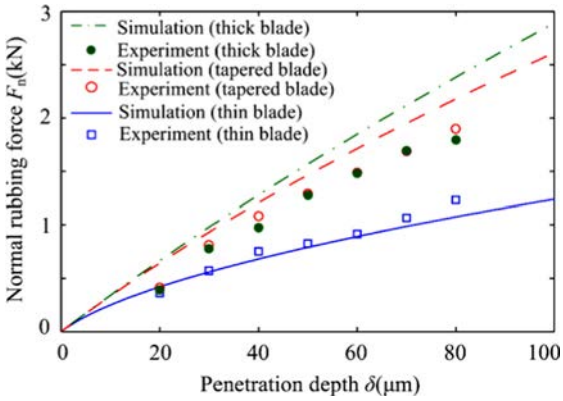

Fig. 13. Normal rubbing forces of different types of blade under different penetration depths (Ω=1000 rev/min, steel casing).

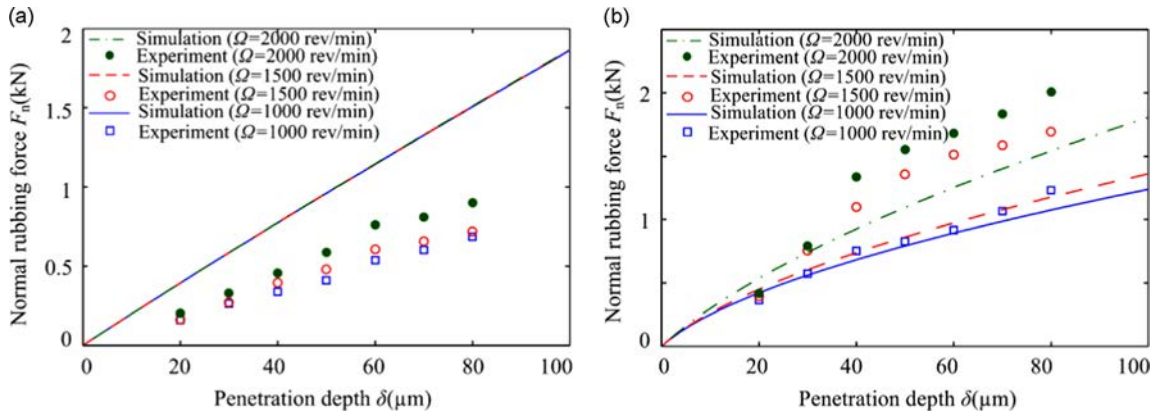

Fig. 14. Normal rubbing force under different penetration depths at different rotating speeds (thin blade): (a) aluminum casing, (b) steel casing.

(3) Comparing with three types of blades, it is clear that the rubbing forces of thick and tapered blade tend to linear change. However, the rubbing force of thin blade tends to nonlinear change due to the large bending deformation of the blade.

3.3.2. Effects of different casing stiffness on the normal rubbing force

In current study, the casing stiffness is adjusted by changing the casing materials. Steel and aluminum casings are selected (see Fig. 8). Moreover, the thin blade is selected to study the effects of rotating speeds and casing stiffnesses on the normal rubbing force. Fig. 14 shows the normal rubbing force under aluminum and steel casings at different rotating speeds. The figure shows the change laws of normal rubbing force as follows:

(1) For the aluminum casing, the simulation results show that the normal rubbing force depends linearly on penetration depth and the rotating speed has almost no effect on the normal rubbing force. The measured results are all less than the simulated results.
(2) For the steel casing, the simulated results show that the normal rubbing force increases with the increasing rotating speed, and the nonlinear relation to penetration depth is obvious. The measured results are close to the simulated results under small penetration depth. The measured results are greater than the simulated results under large penetration depth and the error of both increases with the increasing penetration depths.
(3) The experimental results all show that the normal rubbing force increases with the increasing rotating speed, which is the same as the simulation results. The approximate linear rubbing force reflects that the blade bending deformation is small, and the nonlinear rubbing force indicates that the blade bending deformation is large, which exhibits that the blade bending deformation depends on the casing stiffness.

3.3.3. Comparison of different rubbing force models and experiment

Considering the effects of the blade physical dimensions (thin and thick blades), casing stiffness (aluminum and steel casings) and rotating speeds (1000, 1500 and 2000 rev/min), the comparisons of simulation results obtained by three

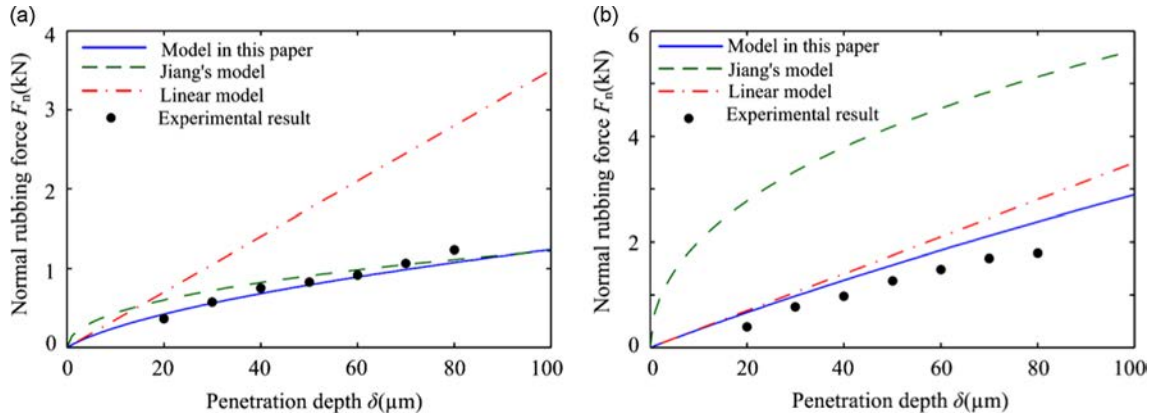

Fig. 15. Comparison of different rub-impact force models with different thicknesses of the blade (steel casing, Ω=1000 rev/min): (a) thin blade, (b) thick blade.

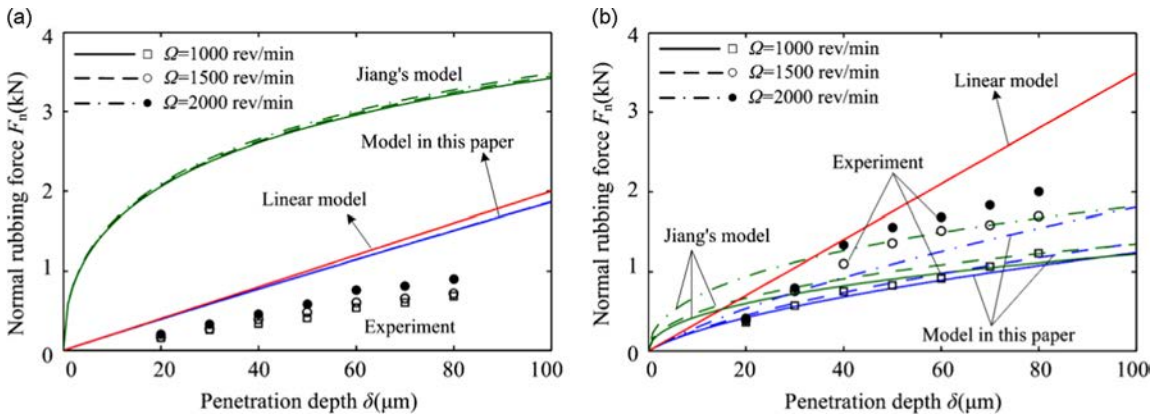

Fig. 16. Comparison of different rubbing force models under different rotating speeds (thin blade): (a) aluminum casing, (b) steel casing.

theoretical models and experimental results are performed, as are shown in Figs. 15 and 16. These figures show the following laws:

(1) For the thin blade, Jiang's model (Eq. (3)) and our model fit together well with the measured results due to the stiffness of thin blade smaller than that of the steel casing (see Fig. 15a). For the thick blade, its stiffness is close to or greater than the casing stiffness. Under this condition, Jiang's model is unsuitable due to the assumption of rigid casing, and our model and linear model (Eq. (1)) are relatively close to the experimental results (see Fig. 15b).
(2) For thin blade, the stiffness of the aluminum casing is relatively small, so the similar law can be observed by comparing Fig. 15b with Fig. 16a. For steel casing, Jiang's model and our model are relatively close to the experimental results (see Fig. 16b). Under large penetration depths, Jiang's model is more close to the measured results. The main error reason for our model is that the casing stiffness evaluation is not necessarily precise and the measured penetration depths may not be completely accurate. This also indicates that casing stiffness is a key parameter to determine the normal rubbing force.

4. Dynamic normal rubbing force analysis under the blade-casing rubbing

Above simulated rubbing forces are all based on the quasi-static hypothesis. In order to further verify the validity of the normal rubbing expression under many supposition conditions, the dynamic normal rubbing force will be obtained under more reasonable assumptions in this section.

4.1. Dynamic model of blade

Based on the physical dimension of the uniform-section blade, a rotating blade model consisted of a flexible beam cantilevered on a rigid disk is established to calculate the system vibration responses under blade-casing condition (see Fig. 17). In the figure, the position of the blade is described by two coordinate frames: a global coordinate system *OXYZ*,

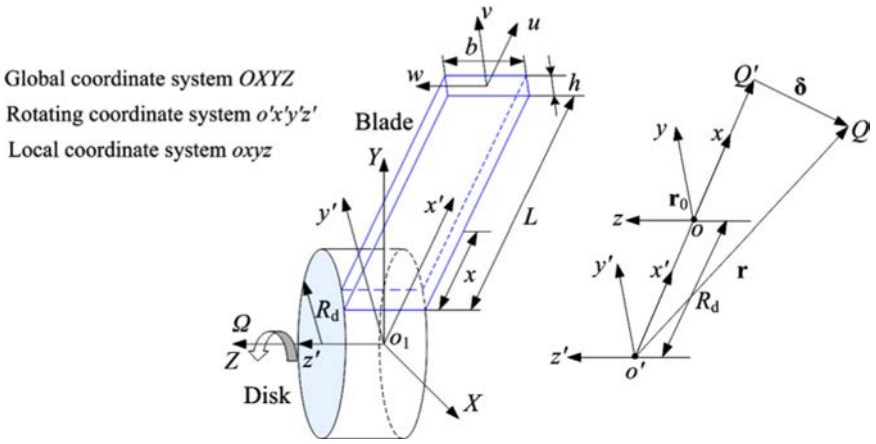

Fig. 17. Schematic diagram of a rotating beam.

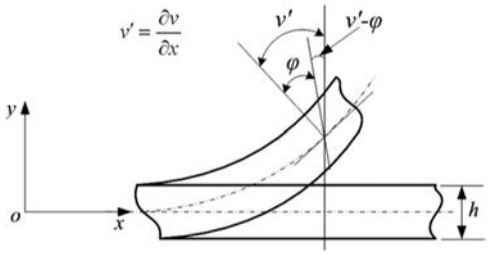

Fig. 18. Schematic diagram of Timoshenko beam.

a rotating coordinate system $o'x'y'z'$ fixed to the central line of the disk and a local coordinate system $oxyz$. u, v and w represent the displacements in radial, lateral and swing directions of the blade at the local coordinate system $oxyz$.

Displacement vector $\mathbf{r}$ of a point Q in rotating coordinate system $o'x'y'z'$ can be expressed as:

$$\mathbf{r}=\mathbf{r}_0+\boldsymbol{\delta}=\begin{bmatrix} R_{\mathrm{d}}+x+u \\ v \\ 0 \end{bmatrix},\ \mathbf{r}_0=\begin{bmatrix} R_{\mathrm{d}}+x \\ 0 \\ 0 \end{bmatrix},\ \boldsymbol{\delta}=\begin{bmatrix} u \\ v \\ w \end{bmatrix}. \tag{20}$$

The blade is simulated by Timoshenko beam, which can consider the effect of shear deformation (see Fig. 18). In the figure, φ is the shear angle in blade local coordinate system. Vector $\boldsymbol{r}_{\mathrm{Q}}$ in global coordinate system $OXYZ$ corresponding to $\boldsymbol{r}$ in rotating coordinate system $o'x'y'z'$ can be written as

$$\mathbf{r}_{\mathrm{Q}}=\begin{bmatrix} \cos\theta & -\sin\theta & 0 \\ \sin\theta & \cos\theta & 0 \\ 0 & 0 & 1 \end{bmatrix}\begin{bmatrix} R_d+x+u-y\varphi \\ v+y \\ w \end{bmatrix}, \tag{21}$$

where θ is the rotation angular of the disk motion, $\theta=\Omega t$.

In this study, only the axial and bending vibrations of the blade are taken into account, namely $w=0$ and $\dot{w}=0$. The kinetic energy of the blade can be written as:

$$T=\frac{1}{2}\int \dot{\mathbf{r}}_{\mathrm{Q}}^2\mathrm{d}m=\frac{1}{2}\int \rho A\dot{\mathbf{r}}_{\mathrm{Q}}^{\mathrm{T}}\cdot\dot{\mathbf{r}}_{\mathrm{Q}}\mathrm{d}x. \tag{22}$$

The potential energy of the blade simulated by Timoshenko beam considering the effects of bending, compression, transverse shear and centrifugal force as well as the normal rubbing force, is given as

$$V=\frac{1}{2}\int_0^L EI\left(\frac{\mathrm{d}\varphi}{\mathrm{d}x}\right)^2\mathrm{d}x+\frac{1}{2}\int_0^L EA\left(\frac{\mathrm{d}u}{\mathrm{d}x}\right)^2\mathrm{d}x+\frac{1}{2}\int_0^L \kappa AG\left(\frac{\mathrm{d}v}{\mathrm{d}x}-\varphi\right)^2\mathrm{d}x+\frac{1}{2}\int_0^L f_c(x)\left(\frac{\mathrm{d}v}{\mathrm{d}x}\right)^2\mathrm{d}x+\frac{1}{2}F_n\int_0^L\left(\frac{\mathrm{d}v}{\mathrm{d}x}\right)^2\mathrm{d}x, \tag{23}$$

where E, I, G, κ, f_c and F_n are Young's modulus, cross-section inertia moment of the blade, shear modulus, shear correction factor, centrifugal force and normal rubbing force, respectively.

The expression of the centrifugal force of the rotating blade is written as

$$f_c(x)=\int_x^L \mathrm{d}f_c(x)=\frac{1}{2}\rho A\dot{\theta}^2\left(L^2+2R_dL-2R_dx-x^2\right). \tag{24}$$

The work W_{non} done by non-conservative force applied the blade can be expressed as:

$$W_{\text{non}} = \int_0^L F_e \cdot v\mathrm{d}x + F_n u|_{x=L} + F_t v|_{x=L} + T_r \varphi|_{x=L}, \tag{25}$$

where F_e is aerodynamic force in y direction, F_t tangential rubbing force, T_r bending moment at blade tip.

Based on Hamilton principle, the motion equation of the blade can be derived by:

$$\delta \int_{t_1}^{t_2} (T - V + W_{\text{non}})\mathrm{d}t = 0. \tag{26}$$

Substituting kinetic energy expressions Eq. (22) and potential energy expressions Eq. (23) into the expression of Hamilton's principle $\delta \int_{t_1}^{t_2} (T - V + W_{\text{non}})\mathrm{d}t = 0$, and taking δu, δv, $\delta\varphi$ and $\delta\theta$ as independence variables to carry out variational operation, the motion equation of the blade can be formulated as follows:

$$\rho \int_0^L A\ddot{u}\mathrm{d}x - 2\rho \int_0^L A\dot{\theta}\dot{v}\mathrm{d}x - \rho \int_0^L A\dot{\theta}^2 u\mathrm{d}x - \rho \int_0^L A\ddot{\theta}v\mathrm{d}x + EAu'|_{x=L} - \int_0^L E(A'u' + Au'')\mathrm{d}x = \rho \int_0^L A(R_d + x)\dot{\theta}^2\mathrm{d}x + F_n. \tag{27}$$

$$\begin{aligned} &\rho \int_0^L A\ddot{v}\mathrm{d}x + 2\rho \int_0^L A\dot{\theta}\dot{u}\mathrm{d}x - \rho \int_0^L \dot{\theta}^2 v\mathrm{d}x + \rho \int_0^L A\ddot{\theta}u\mathrm{d}x + \kappa GA(v' - \varphi)|_{x=L} - \int_0^L \kappa G(A'v' + Av'')\mathrm{d}x + \int_0^L \kappa G(A'\varphi + A\varphi')\mathrm{d}x \\ &\quad - \int_0^L (f_c'(x)v' + f_c(x)v'')\mathrm{d}x + F_n v'|_{x=L} - \int_0^L (F_n v'' + F_n' v')\mathrm{d}x \\ &\quad = -\rho \int_0^L A(R_d + x)\ddot{\theta}\mathrm{d}x + \int_0^L F_e\mathrm{d}x + F_t. \end{aligned} \tag{28}$$

$$\rho \int_0^L I\ddot{\varphi}\mathrm{d}x - \rho \int_0^L I\dot{\theta}^2\varphi\mathrm{d}x + EI\varphi'|_{x=L} - \int_0^L E(I'\varphi' + I\varphi'')\mathrm{d}x + \int_0^L \kappa GA\varphi\mathrm{d}x - \int_0^L \kappa GAv'\mathrm{d}x = -\rho \int_0^L I\ddot{\theta}\mathrm{d}x + T_r. \tag{29}$$

Assumed modes method is used to discrete each direction deformation of the blade (see Eqs. (27)–(29)). By introducing canonical coordinates $U_i(t)$, $V_i(t)$ and $\psi_i(t)$, the longitudinal displacement $u(x,t)$, lateral displacement $v(x,t)$ and shear angle $\varphi(x,t)$ can be written as

$$\begin{aligned} u(x,t) &= \sum_{i=1}^{n} \phi_{1i}(x)U_i(t) \\ v(x,t) &= \sum_{i=1}^{n} \phi_{2i}(x)V_i(t) \\ \varphi(x,t) &= \sum_{i=1}^{n} \phi_{3i}(x)\psi_i(t) \end{aligned}, \tag{30}$$

where $\phi_{1i}(x)$, $\phi_{2i}(x)$ and $\phi_{3i}(x)$ are the ith modal shape function for longitudinal vibration, lateral vibration and shear angle, respectively, whose expressions are as follows [13]:

$$\begin{cases} \phi_{1i}(x) = \sin(\alpha_i x) \\ \phi_{2i}(x) = \frac{1 - \cos(\alpha_i x)}{\alpha_i} \\ \phi_{3i}(x) = \frac{\sin(\alpha_i x)}{\alpha_i} \end{cases}, \tag{31}$$

where $\alpha_i = ((2i-1)\pi/2L)(i = 1, 2, 3, \ldots, n)$, here n is the number of modal truncation. Substituting Eqs. (30) and (31) into Eqs. (27)–(29), the motion equations of the blade can be written as:

$$\mathbf{M}_b\ddot{\mathbf{q}}_b + (\mathbf{G}_b + \mathbf{D}_b)\dot{\mathbf{q}}_b + (\mathbf{K}_e + \mathbf{K}_c + \mathbf{K}_s + \mathbf{K}_{\text{acc}} + \mathbf{K}_F)\mathbf{q}_b = \mathbf{F}, \tag{32}$$

where $\mathbf{M}_b$, $\mathbf{G}_b$, $\mathbf{D}_b$, $\mathbf{K}_e$, $\mathbf{K}_c$, $\mathbf{K}_s$, $\mathbf{K}_{\text{acc}}$ and $\mathbf{K}_F$ are mass matrix, Coriolis force matrix, damping matrix, structural stiffness matrix, stress stiffening matrix, spin softening matrix, stiffness matrix caused by acceleration, stiffness matrix caused by external force. $\mathbf{q}_b$ and $\mathbf{F}$ are canonical coordinates vector and external force vector. The expressions of these matrixes and vectors can be found in Appendix A.

4.2. Dynamic model of casing

Rubbing is a very complicated process, in which the penetration depth is not only related to the vibration of blade but also related to the casing vibration. In this paper, it is assumed that the elongation of the blade caused by centrifugal force is neglected and the rubbing occurs due to the static misalignment ($g_0 + \delta_{\max}$, $g_0 = R_c - r_g$) between the center of disk and the center of casing (see Fig. 19), R_c the radius of the casing, and $r_g = L + R_d$ the radius of the blade tip orbit. A geometric relationship can be written as

$$\overline{AB}^2 + \overline{oB}^2 = \overline{oA}^2, \tag{33}$$

namely,

$$((r_g-\delta)\sin(\Omega t+\varphi_1))^2+(g_0+\delta_{\max}+(r_g-\delta)\cos(\Omega t+\varphi_1))^2={R_c}^2, \tag{34}$$

where φ_1 the phase position. Finally, δ can be expressed as

$$\delta=r_g+(g_0+\delta_{\max})\cos(\Omega t+\varphi_1)-\sqrt{((g_0+\delta_{\max})\cos(\Omega t+\varphi_1))^2-(g_0+\delta_{\max})^2+R_c^2}. \tag{35}$$

Based on the casing shape of the test rig, some simplifications about the casing are introduced as follows:

(1) Only the rubbing in horizontal direction is considered because the rubbing region is very small, which is similar to fixed-point rubbing or local rubbing, and the stiffness of casing in vertical direction is large.
(2) The casing is considered as a mass-spring-damper system with a single degree of freedom (see Fig. 19). The motion equations of the casing can be written as

$$m_c\ddot{u}_c+c_c\dot{u}_c+k_cu_c=F_n\ \cos(\Omega t+\varphi_1), \tag{36}$$

where m_c, c_c and u_c are mass, damping and displacement of the casing in X direction respectively. In this study, parameters of the casing are listed in Table 4.

4.3. Dynamic normal rubbing force of rotating blade

Simulated dynamic normal rubbing forces of thin blade between two types of casings are shown in Fig. 20 under $\Omega=1000$ rev/min and $\delta_{\max}=50$ μm. These figures show the following laws:

(1) The elastic deformation compatibility condition occurs in the whole rubbing process, and can be approximatively written as $\delta_1\approx u-u_c+\delta$, where δ_1 is the dynamic penetration depth and u the radical displacement of blade. The magnitudes and shapes of normal rubbing force changes with δ_1.
(2) The magnitudes and shapes of normal rubbing force between two types of casings are different, the magnitude of normal rubbing force can be determined by the maximum δ_1 and the shapes of normal rubbing force are similar with the shapes of δ_1. The maximum dynamic normal rubbing force under steel casing is larger than that under aluminum casing.

The thin blade is selected to study the effects of rotating speeds and casing stiffnesses on the maximum dynamic normal rubbing force. Fig. 21 shows the maximum dynamic normal rubbing force under aluminum and steel casings at different rotating speeds. These figures show the change laws of normal rubbing force.

(1) For aluminum casing, the simulated results show that the maximum dynamic normal rubbing force depends approximatively linearly on penetration depth. Different aluminum casing stiffnesses have a great influence on the

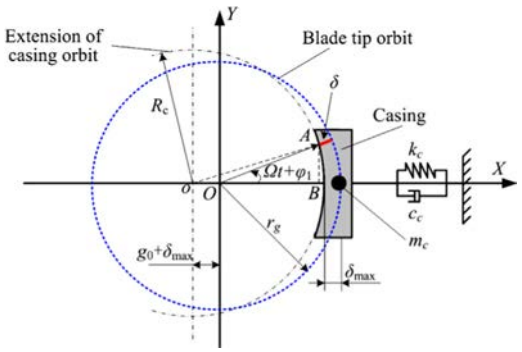

Fig. 19. Schematic of rubbing between the blade and casing.

Table 4
Parameters of the casing.

Material	Aluminum	Steel
Mass of the casing m_c (kg)	1.92	3.02
Damping of the casing c_c (Ns/m)	1×10^3	
Radius of the casing R_c (m)	0.224	

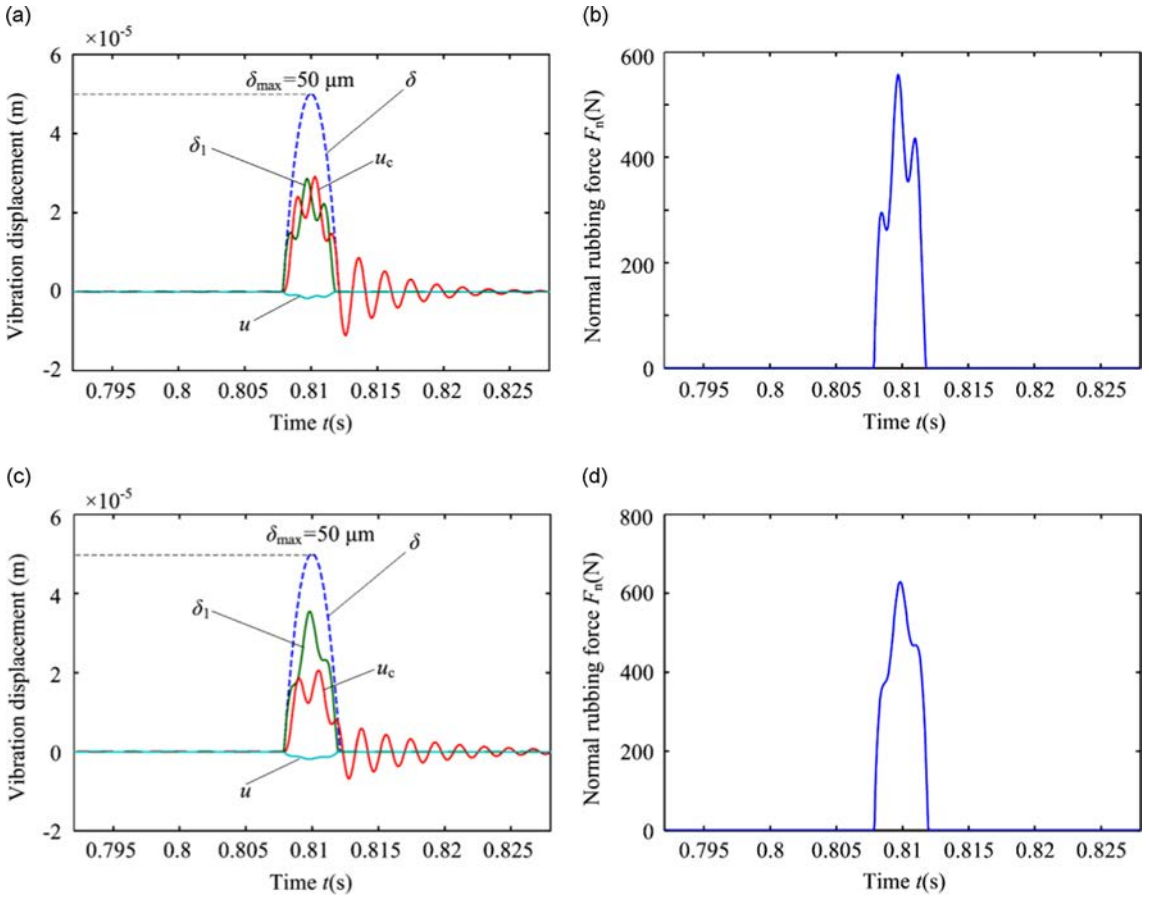

Fig. 20. Vibration displacements of rotating blade (thin blade, Ω=1000 rev/min, δ_{max}=50 μm): (a) displacement response under aluminum casing, (b) normal rubbing force under aluminum casing, (c) displacement response under steel casing, (d) normal rubbing force under steel casing.

maximum dynamic normal rubbing force, and simulation results with appropriate aluminum casing stiffness fit together well with the measured results.

(2) For steel casing, the simulated results show that the maximum dynamic normal rubbing force increases with the increasing rotating speed and nonlinear relation to δ is obvious under large penetration depth. Different steel casing stiffnesses have relatively small influence on the maximum dynamic normal rubbing force, and the measured results are greater than the simulated results under large penetration depth and the error of both increases with the increasing penetration depths.

(3) The quasi-static normal rubbing force is greater than the dynamic normal rubbing force, the main error reason is that the elastic deformation compatibility condition occurs in the whole rubbing process and the real penetration depth is δ_1, however, δ_{max} is adopted in quasi-static normal rubbing force (see Fig. 20).

5. Conclusions

In this study, a new rubbing model between the rotating blade and elastic casing is derived based on the law of conservation of energy. In this model, the bending deflection of blade and the casing deformation during rubbing are considered. The effects of blade physical dimensions, casing stiffnesses, penetration depths and rotating speeds on the quasi-static and dynamic normal rubbing forces are analyzed by simulation and experiment. Some conclusions can be summarized as follows:

(1) A revised rubbing model considering the effects of the elastic casing is presented. By adjusting the casing stiffness, this model is also suitable under elastic and rigid casing conditions. The rubbing model has satisfactory accuracy under some conditions by comparing simulation with experiment.

(2) The linear or nonlinear characteristic of normal rubbing force depends on the stiffnesses of the blade and the casing. When the casing stiffness is greater than the blade stiffness, the normal rubbing force has the nonlinear characteristic relative to penetration depth. Under this condition, the blade deformation dominates the normal rubbing force. When

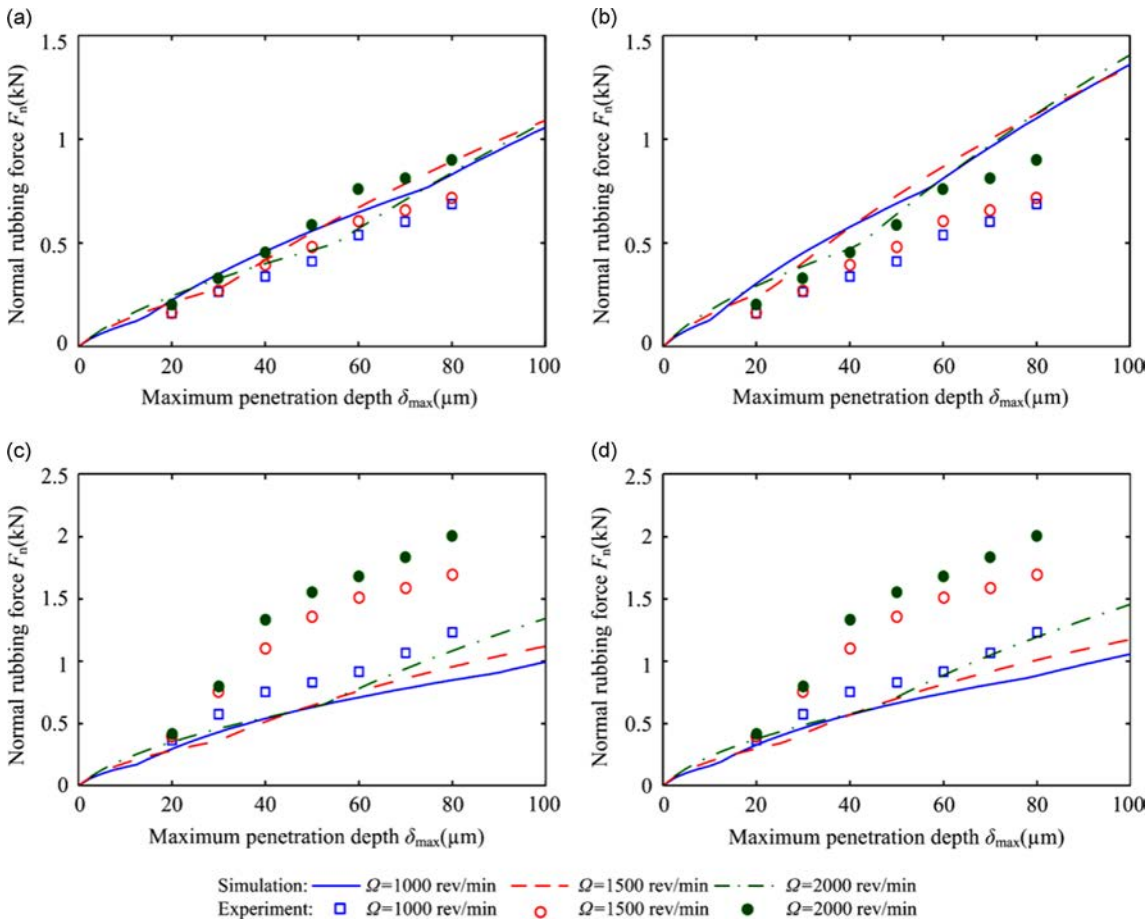

Fig. 21. Maximum dynamic normal rubbing force under different penetration depths at different rotating speeds (thin blade): (a) aluminum casing (2×10^7 N/m), (b) aluminum casing (2.6×10^7 N/m), (c) steel casing (3.5×10^7 N/m), (d) steel casing (4.0×10^7 N/m).

the casing stiffness is less than the blade stiffness, the normal rubbing force has the linear characteristic relative to penetration depth. Under this condition, the casing deformation dominates the normal rubbing force.

(3) Due to the elastic deformation compatibility condition, the quasi-static normal rubbing force is greater than the dynamic normal rubbing force, but both have the same changing trend. The maximum dynamic normal rubbing force depends approximatively linearly on penetration depth under small casing stiffness, and depends nonlinearly on penetration depth under large casing stiffness.

It should be pointed out that the exact determination of the casing stiffness is very difficult because the casing system are composed of multiple assembly parts and multiple connect types, such as bolt-on connection and guide screw connection. Moreover, the nonlinear stiffness characteristic of the casing stiffness may appear under larger penetration depths. The casing system stiffness mainly depends on the system stiffness under rigid casing condition and depends on the casing stiffness under elastic casing condition. The accuracy of the casing stiffnesses is also a main reason to cause the error of simulation and experiment.

Conflict of interest

None.

Acknowledgment

This project is supported by Program for New Century Excellent Talents in University (Grant no. NCET-11-0078), the Fundamental Research Funds for the Central Universities (Grant no. N130403006) and the Joint Funds of the National

Natural Science Foundation and the Civil Aviation Administration of China (Grant no. U1433109) for providing financial support for this work. The authors also thank the anonymous reviewers for their valuable comments.

Appendix A. Vectors and matrixes related to the blade

(1) $\mathbf{q}_b$ is the canonical coordinates vector of the blade ($3n$ rows and one column), where

$$\mathbf{q}_b = \left[U_1 \cdots U_i \cdots U_n \;\; V_1 \cdots V_i \cdots V_n \;\; \psi_1 \cdots \psi_i \cdots \psi_n\right]^{\mathrm{T}}. \tag{A.1}$$

(2) $\mathbf{M}_b$ is the mass matrix of the blade ($3n$ rows and $3n$ columns), where

$$\mathbf{M}_b = \mathrm{diag}[\mathbf{M}_1 \;\; \mathbf{M}_2 \;\; \mathbf{M}_3], \tag{A.2}$$

where

$$\mathbf{M}_1(i,j) = \rho \int_0^L A\phi_{1j}\phi_{1i}\mathrm{d}x, \;\; (i = 1,2,\cdots n), (j = 1,2,\cdots n), \tag{A.3}$$

$$\mathbf{M}_2(i,j) = \rho \int_0^L A\phi_{2j}\phi_{2i}\mathrm{d}x, \;\; (i = 1,2,\cdots n), (j = 1,2,\cdots n), \tag{A.4}$$

$$\mathbf{M}_3(i,j) = \rho \int_0^L I\phi_{3j}\phi_{3i}\mathrm{d}x, \;\; (i = 1,2,\cdots n), (j = 1,2,\cdots n). \tag{A.5}$$

(3) $\mathbf{G}_b$ is the Coriolis matrix of the blade ($3n$ rows and $3n$ columns), the expression of element of $\mathbf{G}_b$ is as follows:

$$\mathbf{G}_b(i,j+n) = -2\dot{\theta}\rho \int_0^L A\phi_{2j}\phi_{1i}\mathrm{d}x, \;\; \mathbf{G}_b(i+n,j) = 2\dot{\theta}\rho \int_0^L A\phi_{1j}\phi_{2i}\mathrm{d}x, \tag{A.6}$$

and the surplus elements are all zero.

(4) Rayleigh damping form is applied to determine total damping matrix $\mathbf{D}_b$ and it can be obtained by the following formula [14]:

$$\mathbf{D}_b = \alpha\mathbf{M}_b + \beta\mathbf{K}_b, \tag{A.7}$$

where

$$\begin{cases} \alpha = \frac{4\pi f_{n1}f_{n2}(f_{n1}\xi_2 - f_{n2}\xi_1)}{(f_{n1}^2 - f_{n2}^2)} \\ \beta = \frac{(f_{n2}\xi_2 - f_{n1}\xi_1)}{\pi(f_{n2}^2 - f_{n1}^2)} \end{cases}, \tag{A.8}$$

herein f_{n1} and f_{n2} respectively stand for the first and second natural frequency (Hz) of the blade, and $\xi_1 = 0.01$, $\xi_2 = 0.02$ are corresponding modal damping ratios, respectively.

(5) $\mathbf{K}_e$ is the structural stiffness matrix of the blade ($3n$ rows and $3n$ columns), the expression of element of $\mathbf{K}_e$ is as follows:

$$\mathbf{K}_e(i,j) = -E\int_0^L \left(A'\phi'_{1j} + A\phi'_{1j}\right)\phi_{1i}\mathrm{d}x + EA\phi'_{1j}\phi_{1i}\Big|_{x=L}, \tag{A.9}$$

$$\mathbf{K}_e(i+n,j+n) = -\kappa G\int_0^L \left(A'\phi'_{2j} + A\phi''_{2j}\right)\phi_{2i}\mathrm{d}x + \kappa GA\phi'_{2j}\phi_{2i}\Big|_{x=L}, \tag{A.10}$$

$$\mathbf{K}_e(i+n,j+2n) = \kappa G\int_0^L \left(A'\phi_{3j} + A\phi'_{3j}\right)\phi_{2i}\mathrm{d}x - \kappa GA\phi_{3j}\phi_{2i}\Big|_{x=L}, \tag{A.11}$$

$$\mathbf{K}_e(i+2n,j+n) = -\kappa G\int_0^L A\phi'_{2j}\phi_{3i}\mathrm{d}x, \tag{A.12}$$

$$\mathbf{K}_e(i+2n,j+2n) = \kappa G\int_0^L A\phi_{3j}\phi_{3i}\mathrm{d}x - E\int_0^L \left(I'\phi'_{3j} + I\phi''_{3j}\right)\phi_{3i}\mathrm{d}x + EI\phi'_{3j}\phi_{3i}\Big|_{x=L}, \tag{A.13}$$

and the surplus elements are all zero.

(6) $\mathbf{K}_c$ is the stress stiffness matrix of the blade ($3n$ rows and $3n$ columns), the expression of element of $\mathbf{K}_c$ is as follows:

$$\mathbf{K}_c(i+n,j+n) = -\int_0^L \left(f'_c(x)\phi'_{2j} + f_c(x)\phi''_{2j}\right)\phi_{2i}\mathrm{d}x, \tag{A.14}$$

and the surplus elements are all zero.

(7) $\mathbf{K}_s$ is the spin softening matrix of the blade ($3n$ rows and $3n$ columns), the expression of element of $\mathbf{K}_s$ is as follows:

$$\mathbf{K}_s(i,j) = -\dot{\theta}^2 \rho \int_0^L A\phi_{1j}\phi_{1i}\mathrm{d}x, \tag{A.15}$$

$$\mathbf{K}_s(i+n,j+n) = -\dot{\theta}^2 \rho \int_0^L A\phi_{2j}\phi_{2i}\mathrm{d}x, \tag{A.16}$$

$$\mathbf{K}_s(i+2n,j+2n) = -\dot{\theta}^2 \rho \int_0^L I\phi_{3j}\phi_{3i}\mathrm{d}x, \tag{A.17}$$

and the surplus elements are all zero.

(8) $\mathbf{K}_{\mathrm{acc}}$ is the stiffness matrix of blade caused by acceleration ($3n$ rows and $3n$ columns), the expression of element of $\mathbf{K}_{\mathrm{acc}}$ is as follows:

$$\mathbf{K}_{\mathrm{acc}}(i,j+n) = -\rho\ddot{\theta} \int_0^L A\phi_{2j}\phi_{1i}\mathrm{d}x, \tag{A.18}$$

$$\mathbf{K}_{\mathrm{acc}}(i+n,j) = \rho\ddot{\theta} \int_0^L A\phi_{1j}\phi_{2i}\mathrm{d}x, \tag{A.19}$$

and the surplus elements are all zero.

(9) $\mathbf{K}_F$ is the stiffness matrix of the blade caused by external force ($3n$ rows and $3n$ columns), the expression of element of $\mathbf{K}_F$ is as follows:

$$\mathbf{K}_F(i+n,j+n) = F_n\left(\phi'_{2j}\phi_{2i}\right)\Big|_{x=L} - \int_0^L \left(F_n\phi''_{2j} + F'_n\phi'_{2j}\right)\phi_{2i}\mathrm{d}x, \tag{A.20}$$

and the surplus elements are all zero.

(10) $\mathbf{F}$ is canonical external force vector of the blade ($3n$ rows and one column), where

$$\mathbf{F} = \begin{bmatrix} \vdots \\ \rho\dot{\theta}^2 \int_0^L A(R_d+x)\phi_{1i}\mathrm{d}x \\ \vdots \\ \int_0^L F_e\phi_{2i}\mathrm{d}x - \rho\ddot{\theta}\int_0^L A(R_d+x)\phi_{2i}\mathrm{d}x \\ \vdots \\ -\rho\ddot{\theta}\int_0^L I\phi_{3i}\mathrm{d}x \\ \vdots \end{bmatrix} + \begin{bmatrix} \vdots \\ F_n\phi_{1i}|_{x=L} \\ \vdots \\ F_t\phi_{2i}|_{x=L} \\ \vdots \\ T_r\phi_{3i}|_{x=L} \\ \vdots \end{bmatrix}. \tag{A.21}$$

References

[1] A. Muszynska, Rotor to stationary element rub-related vibration phenomena in rotating machinery–literature survey, *Shock and Vibration Digest* 21 (1989) 3–11.

[2] S. Ahmad, Rotor casing contact phenomenon in rotor dynamics-literature survey, *Journal of Vibration and Control* 16 (2010) 1369–1377.

[3] Y.S Chen, H.B. Zhang, Review and prospect on the research of dynamics of complete aero-engine systems, *Acta Aeronautica et Astronautica Sinica* 32 (2011) 1371–1391.

[4] J. Jiang, Y.H. Chen, Advances in the research on nonlinear phenomena in rotor/stator rubbing systems, *Advances in Mechanics* 43 (2013) 132–148.

[5] G. Jacquet-Richardet, M. Torkhani, P. Cartraud, F. Thouverez, T. Nouri-Baranger, M. Herran, C. Gibert, S. Baguet, P. Almeida, L. Peletan, Rotor to stator contacts in turbomachines. Review and application, *Mechanical Systems and Signal Processing* 40 (2013) 401–420.

[6] J. Ahrens, H. Ulbrich, G. Ahaus, Measurement of contact forces during blade rubbing, Vibrations in rotating machinery, *Proceedings of the Seventh International Conference*, Nottingham, ImechE, London 2000 pp. 259–268.

[7] J. Padovan, F.K. Choy, Nonlinear dynamics of rotor/blade/casing rub interactions, *Journal of Turbomachinery* 109 (1987) 527–534.

[8] J. Jiang, J. Ahrens, H. Ulbrich, E. Scheideler, A contact model of a rotating, rubbing blade, *Proceedings of the Fifth International Conference on Rotor Dynamics of the IFTOMM*, Darmstadt, Germany 1998, pp. 478–489.

[9] C. Padova, J. Barton, M.G. Dunn, S. Manwaring, G. Young, M. Adams, Development of an experimental capability to produce controlled blade tip/shroud rubs at engine speed, *Journal of Turbomachinery* 127 (2005) 726–735.

[10] C. Padova, J. Barton, M.G. Dunn, S. Manwaring, Experimental results from controlled blade tip/shroud rubs at engine speed, *Journal of Turbomachinery* 129 (2007) 713–723.

[11] C. Padova, M.G. Dunn, J. Barton, K. Turner, A. Turner, D. DiTommaso, Casing treatment and blade-tip configuration effects on controlled gas turbine blade tip/shroud rubs at engine conditions, *Journal of Turbomachinery* 133 (2011) 011016.1–011016.12.

[12] J. Jiang, Investigation of Friction in Blade, Casing Rub and its Effect on Dynamics of a Rotor With Rubs, (Phd Thesis), Shaker Verlag, 2001.

[13] S.K. Sinha, Non-linear dynamic response of a rotating radial Timoshenko beam with periodic pulse loading at the free-end, *International Journal of Non-Linear Mechanics* 40 (2005) 113–149.

[14] K. Bathe, E. Wilson, *Numerical Methods in Finite Element Analysis*, Prentice-Hall, Inc., New Jersey, 1976.